

Effects of Co doping on the structure and physicochemical properties of hausmannite (Mn_3O_4) and its transformation during aging

Shuang Zhang, Hui Li, Zhongkuan Wu, Jeffrey E. Post, Bruno Lanson, Evert J. Elzinga, Yurong Liu, Haigang Li, Mei Hong, Fan Liu, et al.

▶ **To cite this version:**

Shuang Zhang, Hui Li, Zhongkuan Wu, Jeffrey E. Post, Bruno Lanson, et al.. Effects of Co doping on the structure and physicochemical properties of hausmannite (Mn_3O_4) and its transformation during aging. Chemical Geology, 2021, 582, pp.120448. 10.1016/j.chemgeo.2021.120448 . insu-03411470

HAL Id: insu-03411470

https://insu.hal.science/insu-03411470

Submitted on 3 Nov 2021

HAL is a multi-disciplinary open access archive for the deposit and dissemination of scientific research documents, whether they are published or not. The documents may come from teaching and research institutions in France or abroad, or from public or private research centers.

L'archive ouverte pluridisciplinaire **HAL**, est destinée au dépôt et à la diffusion de documents scientifiques de niveau recherche, publiés ou non, émanant des établissements d'enseignement et de recherche français ou étrangers, des laboratoires publics ou privés.

Effects of Co doping on the structure and physicochemical properties of hausmannite (Mn_3O_4) and its transformation during aging

Shuang Zhang[a,b], Hui Li[c], Zhongkuan Wu[d], Jeffrey E. Post[e], Bruno Lanson[f], Evert J. Elzinga[g], Yurong Liu[a,b], Haigang Li[h], Mei Hong[h], Fan Liu[a,b], Hui Yin[a,b,*]

[a]Key Laboratory of Arable Land Conservation (Middle and Lower Reaches of Yangtse River), Ministry of Agriculture and Rural affairs, College of Resources and Environment, Huazhong Agricultural University, Wuhan 430070, China.

[b]State Environmental Protection Key Laboratory of Soil Health and Green Remediation, Ministry of Ecology and Environment, Huazhong Agricultural University, Wuhan 430070, China.

[c]Environmental Sciences Division, Oak Ridge National Laboratory, Oak Ridge, TN 37831

[d]College of Environment, Zhejiang University of Technology, Hangzhou 310014, China

[e]Department of Mineral Sciences, NHB 119, Smithsonian Institution, Washington DC 20013-7012, USA

[f]Univ. Grenoble Alpes, Univ. Savoie Mont Blanc, CNRS, IRD, Univ. Gustave Eiffel, ISTerre, F-38000 Grenoble, France

[g]Department of Earth and Environmental Sciences, Rutgers University, Newark, NJ 07102, United States

[h]College of Grassland, Resources and Environment, Inner Mongolia Agricultural University, Hohhot 010018, China

Corresponding Authors:

Tel.: +86 27 87280271. Fax: +86 27 87288618.

Email: yinhui666@mail.hzau.edu.cn.

Abstract: Hausmannite is a common low-valence manganese oxide mineral with a distorted spinel structure in surficial sediments. Although natural Mn oxides often contain various transition metal (TM) impurities, few studies have addressed the substitution mechanisms of TMs, such as cobalt (Co), with hausmannite and induced changes in the mineral physicochemical properties. In this study, Co-doped hausmannites with final Co/Mn molar ratios of 0.05 and 0.11 were synthesized and characterized by wet chemical analysis, powder X-ray diffraction (XRD), Fourier transformed infrared spectra (FTIR), high resolution transmission electron microscope (HRTEM), X-ray photoelectron spectroscopy (XPS) and X-ray absorption fine structure spectroscopy (XAFS). Co-doped samples have larger crystallite sizes and smaller specific surface areas than those of the hausmannite without Co. The Co cations exist in a mixed-valence of +3 and +2. Powder XRD and acid dissolution experiments indicate that Co incorporates into the mineral structures, and increases the mineral structural stability. Co K-edge extended X-ray adsorption fine structure (EXAFS) analysis demonstrates that Co likely substitutes for lattice Mn(III). After aging at room temperature for three years, 14.1 ± 1.9% of pure hausmannite is transformed to manganite while only 2.6 ± 0.7% of manganite appears in the aged Co-doped sample with an initial Co/Mn molar ratio of 0.10. These results provide new insights into the incorporation mechanisms of TMs into low valence Mn oxides, and the stability of these minerals in natural environments.

Keywords: Mn oxide, hausmannite, transition metal, cobalt, transformation.

1. Introduction

Manganese (Mn) oxide minerals in various geological settings are often enriched in various transition metals (TMs). Incorporation of TMs into Mn oxides can modify the mineral substructure, physicochemical properties and reactivity towards various pollutants (Song et al., 2020; Yin et al., 2012). Our previous studies on the effects of TMs on the reactivity of hexagonal birnessite towards various pollutants convincingly demonstrate that the reactivity of these TM-containing minerals, which are close to natural analogs, can be much different from those of the pure one. For example, incorporation of Ni into hexagonal birnessite greatly reduces the adsorption densities of heavy metals, Pb^{2+} or Zn^{2+}, on the minerals by 79-85% (Yin et al., 2012). The removal efficiencies of Cr^{3+} from water by Co- and Ni-containing birnessites are 28-55% and 67-78%, respectively, that of the pure birnessite (Yin et al., 2020a).

Hausmannite is not only the fifth most common Mn oxide mineral in soils and sediments, but is also found in hydrothermal and metamorphic deposits (Chartier et al., 1999; Giovannelli et al., 2012; Jarosch, 1987). It has a tetragonally deformed spinel structure, elongated along the *c* axis, with Mn^{2+} occupying the tetrahedral sites and Jahn-Teller active Mn^{3+} in the octahedral sites (Bordeneuve et al., 2010; Jarosch, 1987; Sukhdev et al., 2020). Hausmannite is usually not only the precursor or secondary product of other Mn oxide phases (Barreto et al., 2020; Birkner and Navrotsky, 2012; Birkner and Navrotsky, 2014; Feng et al., 2004), but also can have adsorption and redox reactivity towards a variety of metal pollutants (Barreto et al., 2020; Johnson et al., 2018; Shaughnessy et al., 2003; Song et al., 2020; Wilk et al., 2005).

Being the most widely distributed Mn oxide spinel, hausmannite is capable of housing various substituents, including Co, Ni, Fe and Al (Antao et al., 2019; Baron et al., 1998; Bordeneuve et al., 2010; Green et al., 2004; Lefkowitz and Elzinga, 2015; Rajeesh Kumar et al., 2021; Song et al., 2020). Substitution of Fe^{3+} for Mn^{3+} into the octahedral site in hausmannite decreases the Jahn-Teller distortion, increases the Curie point, and decreases the spontaneous magnetization (Baron et al., 1998). Zn doping changes the morphologies of the obtained hausmannite crystallites from nanorods for the pure mineral to a mixture of nanorods and nanoparticles, and increases the energy

bandgap (Jha et al., 2012). Pb doping greatly reduces the Mn_3O_4 particle size and increases the bandgap, dielectric constant, and AC conductivity (Şahin et al., 2020). Doping with various TMs (Cr^{3+}, Co^{2+}, Ni^{2+}, and Cu^{2+}) greatly enhances the phase stability during cycling and charge-transfer behaviors of hausmannite (Dong et al., 2013). However, these studies mainly focus on the applications of TM-modified hausmannites in materials sciences. It is recently reported that Ni substitution in hausmannite causes noticeable changes in the mineral structure (e.g. lattice parameters), and enhances mineral acid dissolution and oxidation reactivity towards As(III) at pH = 5 (Song et al., 2020). This indicates that structural impurities may modify the structure and physicochemical properties of hausmannite and thus the adsorption and redox reactivity towards pollutants. Unlike Ni, Co is highly redox-sensitive, and the influence of Co incorporation on the reactivity and stability of hausmannite remains to be determined.

Further, as a kind of metastable mineral, hausmannite can be converted into other Mn oxides phases during aging. These processes can be affected by mineral properties, such as chemical composition and particle sizes, and environmental conditions, e.g., moisture, temperature and O_2 (Birkner and Navrotsky, 2012; Birkner and Navrotsky, 2014; Kirillov et al., 2009; Rabiei et al., 2005). At 60% relative humidity at room temperature, hausmannite can change its morphology and chemical identity to manganite (Rabiei et al., 2005). Upon slow oxidation at room temperature for 1 year, the hausmannite content in a mixture of hausmannite with manganite is decreased from 47% to 28% (Kirillov et al., 2009). Small crystallite size is reported to promote hausmannite transformation (Birkner and Navrotsky, 2012; Birkner and Navrotsky, 2014). These previous studies mainly focus on the aging of pure hausmannite. However, the effect of TM doping on the stability of hausmannite and its transformation during aging remains largely unexplored.

The present work aims to investigate the effect of Co doping on the mineral structure, physicochemical properties and stability during aging at room temperature. Specifically, Co-doped hausmannite samples were synthesized at room temperature by a coprecipitation method, and characterized by powder XRD, FTIR and HRTEM. The

valence and crystal chemistry of Mn and Co were investigated by XPS, Co K-edge XAFS and acid dissolution experiments. These findings will help in understanding the effects of TM doping on the structure, properties and stability of low valence Mn oxide minerals in natural environments.

2. Materials and methods

2.1 Preparation of Co-doped hausmannites

Cobalt substituted hausmannite was prepared according to the method described in Giovannelli (Giovannelli et al., 2012). In detail, $CoSO_4 \cdot 7H_2O$ was added to 200 mL of 0.5 M $MnSO_4$ solution to obtain an initial Co/Mn molar ratio of 0, 0.05 and 0.10. After the solution was uniformly mixed, 2 M NaOH solution was added dropwise to keep the suspension pH above 10 for 6 h under stirring in air at room temperature. The pH was recorded by a pH-meter. At the end of the reaction, the slurry was filtered, rinsed with deionized water until the conductivity of filtrate was < 20 $\mu s\ cm^{-1}$ to eliminate the salt excess, and dried at 40 ºC for 3 days, and then ground and sieved (100 mesh). The prepared samples were designated as HM, CoH5, and CoH10 correspondingly.

Portions of the HM and CoH10 powders were stored in closed tubes at room temperature (25 ± 5 ºC) under air condition in the laboratory for three years, and the humidity in laboratory around 50%. The corresponding samples were named as agedHM and agedCoH10.

2.2 Sample characterization

The phase purity of prepared samples was analyzed using a Bruker D8 Advance diffractometer with Cu Kα radiation (λ = 0.15418 nm). The diffractometer was operated at a tube voltage of 40 kV and a tube current of 40 mA in the range of 2θ of 5-85 º at a step of 0.02 º and an integration time of 1.2 s. Rietveld structure refinements were performed using software TOPAS (version 4.2). The specific surface areas (SSA) were measured by N_2 adsorption at liquid nitrogen temperature (77 k) with an Autosorb-1 standard physical adsorption analyzer (Quantachrome Autosorb-1, USA). The samples (100 mg) were degassed under vacuum at 110 ºC for 3 h before N_2 adsorption, and SSA

was calculated by employing the multi-point BET method. HRTEM analysis and selected-area electron diffraction were employed to obtain mineral morphologies, particle sizes, and phase lattice on a JEM-2100F (JEOL, Japan) at 200 keV. The samples were prepared by adding 50 μL of 0.1 $g \cdot L^{-1}$ mineral suspension onto a 200-mesh carbon-coated copper grid (Beijing Zhongjingkeyi Technology Co., Ltd.), and dried at room temperature under air condition. FTIR analyses were performed on a Bruker Equinox 55 model spectrophotometer using KBr pellets with a spectral range of 4000-400 cm^{-1}. XPS of Mn 2p and Co 2p were measured on a VG Multilab 2000 X-ray photoelectron spectrometer with a Mg Kα X-ray source (1253.6 eV) using the large area mode with a pass energy of 25 eV and an energy step size of 0.1 eV. Adventitious C 1s binding energy was used to calibrate the energy and set to 284.8 eV. Data were analyzed using Avantage software, and a Shirley background was used (Yin et al., 2011). For Mn 2p fitting, the fit parameters were used from a previous study (Ilton et al., 2016).

The sample chemical composition was determined via atomic absorption spectrometry (AAS, Varian AAS 240FS) after dissolving 0.1000 g solid in a mixture of 25 mL of 0.25 M $NH_2OH \cdot HCl$ solution and 1 M H_2SO_4 solution. Triplicate analyses were performed. Method blanks and matric spikes were also analyzed along with samples for quality assurance and quality controls, and the spiked recoveries of Mn^{2+} were between 98 and 102% (mean recovery: 100 ± 2%).

2.3 Dissolution experiments

The acid dissolution experiment was performed by adopting the method in our previous study (Qin et al., 2017). Briefly, 0.10 g sample was added into 250 mL of 2 M HCl solution while stirring at a constant rate with a magnetic stir at room temperature. At predetermined time intervals, an aliquot of 5 mL suspension was taken out and immediately filtered through 0.22 μm membrane (Shanghai Xingya purification material factory). The concentration of Mn^{2+} and Co^{2+} in the filtrate were analyzed using AAS. The metal (Me) dissolution ratio was calculated as χ_{Me}= Me(t)/Me(total), where Me (t) is the concentration of metal in solutions at time t, and Me(total) is the final metal concentration after complete dissolution of the mineral.

2.4 X-ray absorption fine structure (XAFS) spectroscopy

The XAFS data were collected at room temperature on the 1W1B beamline at the Beijing Synchrotron Radiation Facility (BSRF) (Yin et al., 2012). Cobalt K-edge XAFS data were collected in florescence mode over the energy range of 7510 to 8305 eV. Reduction and analysis of XAFS data were performed using Athena and Artemis from the IFEFFIT software package (Ravel and Newville, 2006). Cobalt K-edge spectra were background-subtracted using the following parameters: E_0 = 7716 eV, Rbkg = 1.0 Å and k-weight = 2. Structural parameters (bond length (R), coordination number (CN), and Debye-Waller factor (σ^2)) were obtained by fitting the k^3-weighted EXAFS data to the standard EXAFS equation (Kelly et al., 2008). Phase and amplitude functions were calculated using FEFF7.0 (Rehr et al., 1992). The Co K-edge EXAFS data were fitted in an R space of 1-4 Å over a k range of 3.1-12.0 $Å^{-1}$, using several single scattering paths calculated by substituting Co for tetrahedral or octahedral Mn in the hausmannite structure (ICSD 76088). An amplitude reduction factor (S_0^2) of 0.877 for Co was adopted from our previous studies (Yin et al., 2014). In all fits, the number of independent variables was much smaller than that of the independent data points allowed. During Fourier transformation and EXAFS data fitting, a Hanning window was used.

3 Results

3.1 Powder XRD

Three synthesized samples display similar XRD patterns (Fig. 1a), which coincide well with the tetragonal hausmannite standard (ICDD 89-4837). The main characteristic reflections at ~3.10 Å, ~2.77 Å, ~2.49 Å, ~1.58 Å, and ~1.54 Å can be indexed to (112), (103), (211), (321), and (224), respectively (Giovannelli et al., 2012; Zhao et al., 2011). With an increase in Co content, the peak positions of the (*hk*0) reflections do not change but those of (*hkl*) reflections shift to higher angles, indicating a decrease of unit-cell parameter *c*. Rietveld refinements of these samples were performed using the hausmannite structure (ICSD 76088) as the starting model. Because of the similarity of the Co and Mn X-ray scattering factors, the refinements were not able to provide information about ordering of the Co cations over the tetrahedral and octahedral sites

or the Co valence. The refinements were thus carried out assuming all Mn, and the results are listed in Fig. 1a and Table S1. From HM to CoH10, unit-cell parameter *a* is essentially constant at 5.771-5.774 Å, while parameter *c* systematically decreases from 9.477 ± 0.002 Å to 9.370 ± 0.002 Å. The indicator of Jahn-Teller distortion of the [Mn(III)O_6] octahedron in hausmannite, c/(1.414a), likewise decreases from 1.1613 ± 0.0003 for HM to 1.1479 ± 0.0004 for CoH10, indicating the reduction of Jahn-Teller distortion after Co doping (Bordeneuve et al., 2010; Hirai et al., 2016; Kim et al., 2012). In hausmannite, the [Mn(III)O_6] octahedra are elongated along the [001] direction (Jarosch, 1987), therefore the decrease in *c* and the Jahn-Teller distortion indicator clearly confirm the replacement of lattice Mn^{3+} by the smaller $Co^{2+/3+}$ and/or Mn^{4+} (Bordeneuve et al., 2010; Hirai et al., 2016; Shannon, 1976; Song et al., 2020). The coherent scattering domain (CSD) sizes determined by the refinements for HM, CoH5 and CoH10 are 59.1 ± 0.7 nm, 91.6 ± 1.1 nm and 74.9 ± 1.3 nm, respectively. This may suggest that Co doping promotes the hausmannite crystal growth at the experimental conditions.

The powder XRD analysis of three years aged HM (agedHM) and CoH10 (agedCoH10) is plotted in Fig. 1b. In addition to the main reflections of hausmannite (ICSD 76088), there is an additional peak at 2θ of 26.18° in agedHM. This peak coincides well with that of manganite (ICSD 84949). This peak also appears in agedCoH10, but with much lower intensity than that in agedHM. This suggests that Co-doped hausmannite sample undergoes slower oxidation at room temperature during aging in the dry state than that of pure hausmannite. Quantitative phase analysis of these aged samples were performed using the hausmannite (ICSD 76088) and manganite structure (ICSD 84949). The results are depicted in Fig. 1b and Table S2. For agedHM, the contents of hausmannite and manganite are 85.9 ± 1.9%, and 14.1 ± 1.9%, respectively. For agedCoH10, the contents of hausmannite and manganite are 97.4 ± 0.7% and 2.6 ± 0.7%, respectively.

3.2 Elemental analysis, specific surface areas and morphologies

With increasing Co content, the Mn content decreases from 70.92 ± 0.01% for HM to 69.63 ± 0.32% and 65.93 ± 1.16% for CoH5 and CoH10, respectively. The final

Co/Mn molar ratios in these samples are approximately the same as those in the initial reactants. The specific surface area (SSA) of HM is 12.4 $m^2 \cdot g^{-1}$, and decreases to 11.7 $m^2 \cdot g^{-1}$ and 11.8 $m^2 \cdot g^{-1}$ for CoH5 and CoH10, respectively.

Fresh HM crystals are composed of irregular cubic particles (Fig. 2a), which is consistent with previous studies (Giovannelli et al., 2012; Hao et al., 2011; Zhang et al., 2011). Co-doped hausmannite crystals are uniformly composed of cubic particles (Fig. 2b, c), which are also similar to Co-doped hausmannite samples in previous studies (Dong et al., 2013). Statistical analysis of the particle sizes of these samples gives an average size of 85 ± 18 nm of HM, 131 ± 27 nm of CoH5 and 103 ± 28 nm of CoH10 (Fig. S1). These physical sizes coincide well with the CSD sizes obtained by powder XRD analysis. Both suggest that Co-doped samples have larger sizes than the pure one. This may indicate that Co ions play a significant role in the growth and assembly of hausmannite initial crystals, and a low amount of Co may favor the crystal growth of hausmannite; but further increasing the Co content will cause structural defects in the mineral structure and thus retard the crystal growth.

In order to confirm whether these Co-doped hausmannite samples are stable during dry storage at room temperature, the HRTEM and SAED patterns of the samples obtained after aging for 3 years, agedHM and agedCoH10, are also presented in Fig. 2d-i. There are plenty of lath-like crystals in agedHM, besides the cubic crystals (Fig. 2d). The SAED pattern of the cubic crystal (Fig. 2e) confirms that the cubes are pure hausmannite single crystals. In the HRTEM image of the lath crystal (Fig. 2f), a lattice distance of 0.339 nm is observed, matching well with that of manganite. The crystals of agedCoH10 retain their cubic shapes for hausmannite (Fig. 2g), which is also confirmed by HRTEM and SAED (Fig. 2h, i).

3.3 FTIR

The FTIR spectra of these freshly prepared Co-doped hausmannite samples have four peaks located at 408, 525, 629, and 3415 cm^{-1} (Fig. 3). These bands coincide well with those of hausmannite (Kirillov et al., 2009). The 3415 cm^{-1} band is assigned to OH vibrations of physisorbed water molecules, while the three other peaks from left to right correspond to wagging, bending and stretching vibrations of [MnO_6] and [MnO_4] units

(Julien et al., 2004; Kirillov et al., 2009).

After three years aging in the dry state, the spectra of these hausmannites change. Firstly, a peak at 1630 cm^{-1} appears (Fig. 3). As this peak corresponds to molecular H_2O bending vibrations (Kim et al., 2002), the presence of this peak suggests there is a quantity of physisorbed water on the mineral surfaces and/or in the structures. Secondly, although the main peaks for hausmannite are preserved in the spectrum of agedHM, the relative intensities of the peaks belonging to manganite, such as 440, 484, 597, 1085, 1116, 1152, 2075 and 2655 cm^{-1} have increased. This indicates a significant portion of hausmannite is transformed into manganite during the aging (Kirillov et al., 2009; Kohler et al., 1997). Additionally, careful inspection of the spectrum of agedCoH10 shows that, the original 525 cm^{-1} peak of fresh CoH10 is shifted to 508 cm^{-1} for agedCoH10, and there are three small additional peaks at 1085, 1116 and 1152 cm^{-1}, indicating the presence of a minor amount of manganite (Fig. 3e-h). This agrees well with the XRD analysis. Additionally, the bands for agedHM and agedCoH10 are weaker and broader relative to the initial samples, owing to the coexistence of several Mn oxide phases.

3.4 Mn 2p XPS spectra

Manganese 2p spectra of these samples are used to investigate the proportions of various Mn species on the mineral surfaces. With Co content increasing, the peak binding energy (BE) shifts to low BE side (Fig. 4a). For example, the Mn $2p_{3/2}$ BE is decreased from 641.94 eV for HM to 641.01 eV for CoH10, indicating the decrease of the Mn average oxidation state (AOS). Further quantitative fitting analysis of the spectrum using multiplet parameters (Ilton et al., 2016) are conducted (Fig. 4b, c and Table S3). The HM spectrum can be decomposed to 28% Mn^{2+}, 58% Mn^{3+} and 14% Mn^{4+}. With the increase of the dopant level, the relative proportions of Mn^{3+} and Mn^{4+} are decreased but that of Mn^{2+} is increased. The spectrum of CoH10 can be decomposed to 39% Mn^{2+}, 54% Mn^{3+} and 7% Mn^{4+}. The calculated Mn AOSs are 2.86 ± 0.02 and 2.69 ± 0.02 for HM and CoH10, respectively.

3.5 Acid dissolution experiments

Fig. 5 shows the fraction of dissolved Co or Mn (χ_{Co} or χ_{Mn}) vs. time, and χ_{Co} -χ_{Mn}

curves of the Co-doped samples in 2 M HCl solution at room temperature. For both samples, the χ_{Co} or χ_{Mn} vs. time curves show a fast initial rate, followed by a gradual decrease until the dissolution is complete, and the dissolution of Co is slightly quicker than that of Mn. To obtain the Mn and Co dissolution rate constant (K), Kabai equation, χ_{Metal} =1-exp(-(K*t)^a), is employed to model the dissolution curves (Alvarez et al., 2007; Liu et al., 2019). With Co content increasing, the Mn dissolution rate constant (K_{Mn}) is decreased from 0.2823 ± 0.0301 min^{-1} for CoH5 to 0.2070 ± 0.0175 min^{-1} for CoH10. These results indicate that doping Co makes the mineral structure more stable and more resistant to proton attack. This may be related to the higher bond dissociation energy (BDE) of Co-O (397 ± 9 $kJ \cdot mol^{-1}$) than that of Mn−O (362 ± 25 $kJ \cdot mol^{-1}$) (Lide and "Mickey" Haynes, 2010). According to the BDE, it is expected that Mn cations will be slightly easier to be released out of the lattice than Co cations. In contrast, the dissolution-rate constant of Co is much higher than that of Mn, and increases with increasing the Co content in the sample. The Co dissolution rates (K_{Co}) in these samples are 0.6516 ± 0.0724 min^{-1} for CoH5 and 0.8743 ± 0.0804 min^{-1} for CoH10, respectively. This may suggest that Co may not occupy completely the same lattice sites as Mn. But it should also be noteworthy that, the mineral dissolution in HCl solution is a much complex process, which involves protonation, complexation, and reduction induced dissolutions by Cl^- (Cornell and Schwertmann, 2003). It can be affected by many other factors such as crystal sizes, coexisted cations, H^+ concentration and so on. Particles with smaller crystal sizes are dissolved faster than those with large crystal sizes (Alvarez et al., 2007; Cornell and Schwertmann, 2003). The obtained α values for χ_{Co}-t or χ_{Mn}-t for CoH5 and CoH10 are also the same, confirming the purity of these minerals. Further, the χ_{Co} -χ_{Mn} curves are a little convex with respect to the Y=X line. This suggests Co incorporates into the mineral structures but is slightly preferentially enriched in the rims of the crystals (Qin et al., 2017; Yin et al., 2014).

3.6 Co K-edge XAFS analysis

3.6.1 X-ray adsorption near edge structure (XANES)

The Co K-edge XANES profiles of the two Co-doped hausmannite samples, CoH5

and CoH10, are distinct from but intermediate between those of the reference compounds $CoSO_4$ and CoOOH (Fig. 4d), suggesting a mixed-valence of Co in these samples. Linear combination fitting analysis further quantitatively confirms this (Fig. 4d and Table S4). The results show that CoH5 and CoH10 both contain 66-67% Co^{3+} and 33-34% Co^{2+}. Previous studies reported that Co exists as only Co^{2+} in Co-containing hausmannite ($Mn_{3-x}Co_xO_4$, $0 < x < 1$) samples synthesized under mild alkaline conditions and at high temperature (Bordeneuve et al., 2010; Dong et al., 2013; Hirai et al., 2016). In contrast, the samples used here were synthesized using a coprecipitation method at room temperature and at pH > 10.

3.6.2 EXAFS

The k^3-weighted Co K-edge EXAFS and the corresponding Fourier transformed spectrum (FT) of typical Co-doped sample, CoH10, are different from those of CoOOH and $CoSO_4$ references (Yin et al., 2015), indicating neither CoOOH precipitate nor free Co^{2+} exists (Fig. 6a,b). As both powder XRD analysis and acid dissolution confirm the incorporation of Co into the mineral structures, Co can exist in either an octahedral or a tetrahedral coordination or both. The oscillations of CoH5 and CoH10 are essentially the same (Fig. 6c,d), indicating that Co ions in the two samples have similar coordination environments. The corresponding FTs show two strong backscattering neighbors at $R + \Delta R \sim 1.5$ Å and ~ 2.9 Å. The former corresponds to the first Co-O pair, and the later can be deconvoluted into several Co-Me (Me = Mn and Co) pairs (Bordeneuve et al., 2010).

To obtain more detailed information about the local structures of Co in the Co-doped hausmannite samples, the Co K-edge EXAFS spectra of CoH5 and CoH10 are analyzed with shell-by-shell fits (Fig. 6c, d and Table 1). The results indicate an average Co-O distance of 1.97 ± 0.02 Å, which is slightly longer than those (1.90-1.91 Å) previously reported for octahedral Co^{3+} (Manceau et al., 1997; Yin et al., 2013; Yin et al., 2015), but much shorter than for octahedral Co^{2+} (2.09 Å) (Manceau et al., 1997). This further suggests the coexistence of Co^{3+} and Co^{2+} in the hausmannites. Although cations in tetrahedral coordination, such as Zn^{2+}, typically form shorter distances with the first coordination O (Kwon et al., 2009), the case for Co is complex. It was reported

that in $YBaCo_4O_7$, the average tetrahedral Co-O distance ranges from 1.90-1.92 Å (Valldor and Andersson, 2002). Thus, it is difficult to distinguish octahedral from tetrahedral Co based on Co-O distances alone. The fits also indicate longer Co-Me (Me=Co, Mn) correlations at radial distances of 2.80-2.82, 3.01-3.02, 3.36-3.38 and 3.77-3.78 Å (Table 1). These values correspond to the distances between edge-sharing octahedra in the *a*- and *c*-direction, and corner-sharing octahedron-tetrahedron pairs in the *a*- and *c*-direction, respectively, matching well with those for Co located in the octahedron sites (Table S1). Further, when comparing to the corresponding average Me-Me distances obtained by Rietveld structure refinements (Table S1), these Co-Me distances are shorter, owing to the smaller radius of Co(III) (Shannon, 1976).

EXAFS fittings assuming that all the Co cations occupy the tetrahedral sites are also conducted. An average Co-O distance of 1.96 ± 0.01 Å is derived, which is almost the same as that determined assuming all octahedral Co. An attempt to fit the R + ΔR ~ 2.9 Å peak by combining four paths: two paths for octahedron-tetrahedron corner-sharing pairs in the *a*- and *c*-axis, a path for the nearest tetrahedron-tetrahedron pairs and a Co-O path corresponding to that between the center Mn in a tetrahedron and its second shell O belonging to the corner-sharing octahedron, does not yield a reasonable fit. This suggests that the vast majority of Co cations occupy the octahedral sites in Co-doped hausmannites (Song et al., 2020).

4. Discussion

4.1 Co valence and crystal chemistry in Co-doped hausmannite

Cobalt K-edge XANES analysis showed that Co^{2+} and Co^{3+} coexist in the Co-doped hausmannites. Interestingly, the Co^{3+}/Co^{2+} ratios keep almost the same, ~2, for CoH5 and CoH10. Owing to the high redox potential of Co^{3+}/Co^{2+} pair (E^0 = 1.92 V) (Lide and "Mickey" Haynes, 2010), O_2 and high valence Mn in the mineral, and surface catalytic oxidation may account for the Co^{2+} oxidation. The oxidation of Co^{2+} is highly related to the solution conditions, e.g. pH and temperature. Generally, a high concentration of OH^- and high temperature favors the oxidation (Alvarez et al., 2008; Pozas et al., 2004; Yin et al., 2020b). The coexistence of Co^{2+} and Co^{3+} in the doped

hausmannite samples is similar to that observed in Co-doped goethite samples in our previous study (Yin et al., 2020a), both owing to the low alkalinity and low temperature used. However, in the Co-doped goethite series, the Co^{3+}/Co^{2+} ratio increases with increasing initial Co concentration. This is ascribed to the catalytic oxidation of Co^{2+} on the mineral precursor (e.g. ferrihydrite) surfaces driven by the electric potential energy, which is dependent on the redox cation concentration (Boland et al., 2013; Lan et al., 2017; Yin et al., 2020a). The constant Co^{3+}/Co^{2+} ratio here may possibly be explained by the absence of surface catalytic oxidation behaviors on hausmannite surfaces, because hausmannite is an insulator (Bordeneuve et al., 2010).

Powder XRD, acid dissolution experiments and Co K-edge EXAFS analysis demonstrate that the Co cations are incorporated into the mineral structures. In hausmannite, Mn^{2+} occupies the tetrahedral site while Mn^{3+} occupies the octahedral sites. However, when exotic cations are incorporated into the structure, the crystal chemistry of the exotic cations are complex. Structure analysis of cobalt manganese oxide spinel ($Mn_{3-x}Co_xO_4$) ($0 \leq x \leq 3$) synthesized at 800 °C demonstrates that the tetrahedral Mn is first preferentially substituted by Co for $x < 1$, and then the octahedral Mn is replaced by Co with increasing x value. It also shows that Mn^{2+} and/or Co^{2+} fill the tetrahedral sites while Mn^{3+}, Co^{2+}, low-spin state Co^{3+} and Mn^{4+} occupy the octahedral site (Bordeneuve et al., 2010). For a series of $Mn_{3-x}Co_xO_4$ samples ($0 \leq x \leq 1.5$) synthesized at ~20 °C by coprecipitation of the mixtures of Mn^{2+} and Co^{2+} solution using $NH_3 \cdot H_2O$, the $Mn(III)O_6$ distortion indicator, $c/\sqrt{2}a$, almost overlaps with those for the samples from the previous study when $x < 1$, and Co cations in these samples was thought to solely occupy the tetrahedral sites (Hirai et al., 2016). Comparison of the $c/\sqrt{2}a$ of the Co-doped hausmannite samples in the present study with those from previous studies indicates that there is a good linear relationship between Co content and $c/\sqrt{2}a$ for all these samples when $x < 1$, but the dependence of $c/\sqrt{2}a$ to the sample Co content varies much. The $c/\sqrt{2}a$ of our samples decreases much faster with increasing Co content than that in literatures, with a slope ~ 2 times that of the later (Fig. 7). This may indicate that the crystal chemistry of Co in our samples is not the same as that in the previous studies, owing to the fact that the mineral preparation

method will affect the detailed crystal chemistry of Co (Zhao et al., 2017).

Further, there is a debate in the spin state of the cations in the hausmannite structure. Some literatures reported that in the distorted spinel structure of hausmannite, Mn^{2+} is in the low-spin state (LS) while Mn^{3+} is in the high-spin state (HS) (Bordeneuve et al., 2010; Jarosch, 1987; Nogués and Poix, 1974). However, other studies adopted that Mn^{3+} in hausmannite octahedral sites has a low-spin state while Mn^{2+} in tetrahedral sites has a high-spin state (Boucher et al., 1971; Xu et al., 2005). According to molecular orbital calculations, if the MnO_6^{9-} cluster has smaller exchange splitting of the $2t_{2g}$ orbital and larger crystal field splitting, a transition of Mn(III) from HS to LS can occur, in company with a decrease of Mn-O distance from 2.04 to 1.88 Å (Sherman, 1984). The average Mn-O distances in $[Mn(III)O_6]$ in our Co-doped hausmannites are 2.05-2.06 Å (Table S1). This probably suggests that Mn(III) in our hausmannites are probably HS. In the normal spinel structure of Co_3O_4, HS Co^{2+} occupies the tetrahedral sites while LS Co^{3+} occupies the octahedral sites (Spencer and Schroeer, 1974). In order to elucidate the possible distributions of various cations in these Co-doped hausmannite samples, the basic physicochemical properties of these cations are compared (Table 2).

After Co doping, the proportions of Mn^{3+} and Mn^{4+} are decreased while that of Mn^{2+} is increased with increasing dopant content. It is generally assumed that Co^{3+} in octahedral sites exists mostly in the LS state (Burns, 1993; McKenzie, 1970; Yin et al., 2013). The CFSE of LS Co^{3+} (534.2 $kJ \cdot mol^{-1}$) is ~2.5 times larger than that of Mn^{3+} in the hausmannite structure, and therefore, it is favorable for Co^{3+} to replace Mn^{3+}. This is the same for LS Co^{2+}. The CFSE of octahedrally coordinated LS Co^{2+} (198.2 $kJ \cdot mol^{-1}$) is larger than that of HS Mn^{3+} in hausmannite, favoring the substitution of Mn^{3+} by Co^{2+}. This is supported by the Co K-edge EXAFS analysis. Further, as the radius of LS Co^{3+} in octahedral coordination is 12.7% smaller than that of HS Mn^{3+}, this substitution also accounts for the decrease of unit-cell parameter *c* and the suppression of the Jahn-Teller distortion. Further, the smaller CFSE of tetrahedral HS Co(II) (58.7 $kJ \cdot mol^{-1}$) than that of LS Mn(II) (79.6 $kJ \cdot mol^{-1}$) in tetrahedron excludes the substitution of Co(II) for tetrahedral Mn(II). Consequently, it is assumed that in the Co-doped hausmannite samples low-spin Co^{2+} and Co^{3+} occupy the octahedral sites.

4.2 Hausmannite transformation during aging

After aging the pure hausmannite (HM) and Co-doped hausmannite (CoH10) in dry state for three years, 14.1 ± 1.9% of manganite appears in agedHM while 2.6 ± 0.7% of manganite is observed in agedCoH10. This clearly suggests the transformation of hausmannite to manganite. It is proposed that the transformation of hausmannite to manganite involves O_2 and H_2O according to the following equation (eq. 1):

$$4Mn_3O_4 + O_2(g) + 6H_2O(g) = 12MnOOH \quad (1)$$

During hausmannite aging in dry state, Mn(II) on the mineral surfaces are gradually oxidized by O_2 to form -Mn=O groups. Then these groups react with physisorbed H_2O, leading to the formation of -Mn=$(OH)_2$ groups. Finally -Mn=$(OH)_2$ groups are transformed to MnOOH, which is thought to be the rate-determining step (Kirillov et al., 2009).

This transformation processes can be affected by many factors. In the present study, the O_2 and H_2O concentrations are limited during hausmannite aging, which is stored in a closed tube. Thus the transformation rate here is much lower than those in air (Kirillov et al., 2009) and in high relative humidity(Rabiei et al., 2005). However, the transformation rate of CoH10 is much lower than that of HM at same conditions. This may be related to the substitution-induced changes in mineral physicochemical properties, such as chemical composition, particle size and stability of the host mineral. Although Co-doped hausmannite samples here show the same cubic morphology as that of pure hausmannite, statistical analyses of TEM determined particle sizes and the CSDs obtained by XRD show that the Co-doped crystals are larger than those of HM. The increase in crystal sizes of CoH5 and CoH10 may make them more stable than HM (Birkner and Navrotsky, 2014; Gillot et al., 2001), since smaller crystallite size is reported to promote phase transformation (Birkner and Navrotsky, 2012; Birkner and Navrotsky, 2014). Additionally, doping Co decreases the Mn^{3+} content, and suppresses the Jahn-Teller distortion to make the mineral structure more stable than pure one. The decrease of Mn^{3+} may also favor the formation of hausmannite rather than MnOOH phase (Jha et al., 2012). Our results clearly show that, exotic cation substitution have great impact on the transformation of hausmannite. Conclusively, the enrichment of

various TMs in hausmannite may be an important reason for the stability of these minerals in natural environments.

5. Conclusions and environmental implications

Natural hausmannite analogs, including Co-substituted hausmannites with Co/Mn molar ratios of 0.05 and 0.11 were synthesized at ambient conditions. Cobalt ions existed as Co^{3+} and Co^{2+}, substituting for Mn^{3+} in the octahedral sites, which resulted in suppression of the Jahn-Teller distortion and a commensurate decrease in the unit-cell parameter *c*. These Co-doped hausmannite samples had decreased Mn AOS and increased crystal sizes than HM. Acid dissolution experiments confirmed that Co incorporated into the mineral structures, and made the mineral more stable. Cobalt K-edge EXAFS analysis demonstrated that dopants occupied the octahedral sites in the hausmannite structure. Cobalt doping greatly improved the hausmannite stability during dry aging at room temperature. After three years of aging in a dry state, 14.1 ± 1.9% of hausmannite in HM was transformed to manganite, while only 2.6 ± 0.7% of hausmannite in CoH10 was transformed to manganite.

Based on the excellent adsorption, reducing and oxidizing reactivity towards a variety of metal pollutants (Antao et al., 2019; Baron et al., 1998; Bordeneuve et al., 2010; Green et al., 2004; Lefkowitz and Elzinga, 2015; Song et al., 2020), hausmannite may play an important role in mediating the mobility and fate of metal nutrients and contaminants in terrestrial environments. The substitution of TM for lattice Mn in the hausmannite structure may greatly modify the mineral physicochemical properties and thus their reactivity. Carefully and accurately investigation of the reactivity of these doped minerals, which are close to their natural analogues, with nutrients and pollutants, may help us understand and predict the geochemical behaviors of elements of interest in natural settings and also benefit us from the design and application of environmental-friendly Mn oxide materials in pollutant control and remediation.

Acknowledgments

We gratefully acknowledge Dr. Wei Zhao from Northwest A&F University for providing the FTIR data of manganite. The authors gratefully thank the Key science and technology projects of Inner Mongolia autonomous region (2019ZD001), the National Natural Science Foundations of China (Nos.42077015 and 41771267), the National Key Research and Development Program of China (No. 2016YFD0800403), and the Fundamental Research Funds for the Central Universities (Grant 103-510320036) for the financial support.

REFERENCES

Alvarez, M., Rueda, E.H., Sileo, E.E., 2007. Simultaneous incorporation of Mn and Al in the goethite structure. Geochimica et Cosmochimica Acta, 71(4): 1009-1020.

Alvarez, M., Sileo, E.E., Rueda, E.H., 2008. Structure and reactivity of synthetic Co-substituted goethites. American Mineralogist, 93(4): 584-590.

Antao, S.M., Cruickshank, L.A., Hazrah, K.S., 2019. Structural Trends and Solid-Solutions Based on the Crystal Chemistry of Two Hausmannite (Mn_3O_4) Samples from the Kalahari Manganese Field. Minerals, 9(6): 343.

Baron, V., Gutzmer, J., Rundlof, H., Tellgren, R., 1998. The influence of iron substitution on the magnetic properties of hausmannite, $Mn^{2+}(Fe,Mn)_{(2)}(^{3+})O_4$. American Mineralogist, 83(7-8): 786-793.

Barreto, M.S.C., Elzinga, E.J., Alleoni, L.R.F., 2020. Hausmannite as potential As(V) filter. Macroscopic and spectroscopic study of As(V) adsorption and desorption by citric acid. Environmental Pollution, 262: 114196.

Birkner, N., Navrotsky, A., 2012. Thermodynamics of manganese oxides: Effects of particle size and hydration on oxidation-reduction equilibria among hausmannite, bixbyite, and pyrolusite. American Mineralogist, 97(8-9): 1291-1298.

Birkner, N., Navrotsky, A., 2014. Rapidly reversible redox transformation in nanophase manganese oxides at room temperature triggered by changes in hydration. Proceedings of the National Academy of Sciences, 111(17): 6209-6214.

Boland, D.D., Collins, R.N., Glover, C.J., David Waite, T., 2013. An in situ quick-EXAFS and redox potential study of the Fe(II)-catalysed transformation of ferrihydrite. Colloids and Surfaces A: Physicochemical and Engineering Aspects, 435: 2-8.

Bordeneuve, H. et al., 2010. Structural variations and cation distributions in $Mn_{3-x}Co_xO_4$ ($0 \leqslant x \leqslant 3$) dense ceramics using neutron diffraction data. Solid State Sciences, 12(3): 379-386.

Boucher, B., Buhl, R., Perrin, M., 1971. Proprietes et structure magnetique de Mn_3O_4. Journal of Physics and Chemistry of Solids, 32(10): 2429-2437.

Burns, R.G., 1993. Mineralogical applications of crystal field theory. Cambridge topics in mineral physics and chemistry. Cambridge university press, New York.

Chartier, A., D'Arco, P., Dovesi, R., Saunders, V.R., 1999. Ab initio Hartree-Fock investigation of the structural, electronic, and magnetic properties of Mn_3O_4. Physical Review B, 60(60).

Cornell, R.M., Schwertmann, U., 2003. The iron oxides : structure, properties, reactions, occurences and uses. Wiley-VCH, Weinheim.

536 Dong, R. et al., 2013. Enhanced supercapacitor performance of Mn_3O_4 nanocrystals by doping transition-
537 metal ions. ACS Applied Material & Interfaces, 5(19): 9508-16.
538 Feng, X.H., Liu, F., Tan, W.F., Liu, X.W., 2004. Synthesis of birnessite from the oxidation of Mn^{2+} by O_2
539 in alkali medium: Effects of synthesis conditions. Clays and Clay Minerals, 52(2): 240-250.
540 Gillot, B., El Guendouzi, M., Laarj, M., 2001. Particle size effects on the oxidation–reduction behavior
541 of Mn_3O_4 hausmannite. Materials Chemistry and Physics, 70(1): 54-60.
542 Giovannelli, F. et al., 2012. Synthesis of manganese spinel nanoparticles at room temperature by
543 coprecipitation. Journal of Solid State Chemistry, 192: 109-112.
544 Green, W.J. et al., 2004. Nickel, Copper, Zinc and Cadmium cycling with manganese in Lake Vanda
545 (Wright Valley, Antarctica). Aquatic Geochemistry, 10(3): 303-323.
546 Hao, X. et al., 2011. Mild aqueous synthesis of octahedral Mn_3O_4 nanocrystals with varied oxidation
547 states. Colloids and Surfaces A: Physicochemical and Engineering Aspects, 374(1-3): 42-47.
548 Hirai, S. et al., 2016. Enhancement of the oxygen evolution reaction in Mn^{3+}-based electrocatalysts:
549 correlation between Jahn–Teller distortion and catalytic activity. RSC Advances, 6(3): 2019-
550 2023.
551 Ilton, E.S., Post, J.E., Heaney, P.J., Ling, F.T., Kerisit, S.N., 2016. XPS determination of Mn oxidation
552 states in Mn (hydr)oxides. Applied Surface Science, 366: 475-485.
553 Jarosch, D., 1987. Crystal structure refinement and reflectance measurements of hausmannite, Mn_3O_4.
554 Mineralogy & Petrology, 37(1): 15-23.
555 Jha, A., Thapa, R., Chattopadhyay, K.K., 2012. Structural transformation from Mn_3O_4 nanorods to
556 nanoparticles and band gap tuning via Zn doping. Materials Research Bulletin, 47(3): 813-819.
557 Johnson, K.L. et al., 2018. Dissolved Mn(III) in water treatment works: Prevalence and significance.
558 Water Research, 140: 181-190.
559 Julien, C.M., Massot, M., Poinsignon, C., 2004. Lattice vibrations of manganese oxides: Part I. Periodic
560 structures. Spectrochimica Acta Part A: Molecular and Biomolecular Spectroscopy, 60(3): 689-
561 700.
562 Kelly, S.D., Hesterberg, D., Ravel, B., 2008. Analysis of soils and minerals using X-ray absorption
563 spectroscopy. In: Ulrey, A.L., Drees, R.L. (Eds.), Methods of Soil Analysis, Part 5-
564 MineralogicalMethods. Soil Science Society of America.
565 Kim, H. et al., 2012. Multicomponent effects on the crystal structures and electrochemical properties of
566 spinel-structured M_3O_4 (M = Fe, Mn, Co) anodes in lithium rechargeable batteries. Chemistry
567 of Materials, 24(4): 720-725.
568 Kim, J.G., Dixon, J.B., Chusuei, C.C., Deng, Y.J., 2002. Oxidation of chromium(III) to (VI) by
569 manganese oxides. Soil Science Society of America Journal, 66(1): 306-315.
570 Kirillov, S.A. et al., 2009. Oxidation of synthetic hausmannite (Mn_3O_4) to manganite (MnOOH). Journal
571 of Molecular Structure, 928(1): 89-94.
572 Kohler, T., Armbruster, T., Libowitzky, E., 1997. Hydrogen bonding and Jahn–Teller distortion in
573 groutite,α-MnOOH, and manganite,γ-MnOOH, and their relations to the manganese dioxides
574 ramsdellite and pyrolusite. Journal of Solid State Chemistry, 133(2): 486-500.
575 Kwon, K.D., Refson, K., Sposito, G., 2009. Zinc surface complexes on birnessite: A density functional
576 theory study. Geochimica Et Cosmochimica Acta, 73(5): 1273-1284.
577 Lan, S. et al., 2017. Mechanisms of Mn(II) catalytic oxidation on ferrihydrite surfaces and the formation
578 of manganese (oxyhydr)oxides. Geochimica Et Cosmochimica Acta, 211: 79-96.
579 Lefkowitz, J.P., Elzinga, E.J., 2015. Impacts of aqueous Mn(II) on the sorption of Zn(II) by hexagonal

birnessite. Environmental Science & Technology, 49(8): 4886-4893.
Lide, D.R., "Mickey" Haynes, W.M., 2010. CRC handbook of chemistry and physics. CRC Press, Florida.
Liu, L. et al., 2019. The speciation of Cd in Cd–Fe coprecipitates: Does Cd substitute for Fe in goethite structure? ACS Earth and Space Chemistry, 3(10): 2225-2236.
Manceau, A., Silvester, E., Bartoli, C., Lanson, B., Drits Victor, A., 1997. Structural mechanism of Co^{2+} oxidation by the phyllomanganate buserite, American Mineralogist, pp. 1150.
McKenzie, R., 1970. The reaction of cobalt with manganese dioxide minerals. Soil Research, 8(1): 97-106.
Nogués, M., Poix, P., 1974. Effet Jahn-Teller coopératif dans le système $Mn_3O_4 \cdot Mn_2SnO_4$. Journal of Solid State Chemistry, 9(4): 330-335.
Pozas, R., Rojas, T.C., Ocana, M., Serna, C.J., 2004. The nature of Co in synthetic Co-substituted goethites. Clays and Clay Minerals, 52(6): 760-766.
Qin, Z. et al., 2017. Local structure of Cu^{2+} in Cu-doped hexagonal turbostratic birnessite and Cu^{2+} stability under acid treatment. 466: S0009254117303984.
Rabiei, S. et al., 2005. Conversion of hausmanite (Mn_3O_4) particles to nano-fibrous manganite (MnOOH) at ambient conditions. Journal of Materials Science, 40(18): 4995-4998.
Rajeesh Kumar, N.K., Vasylechko, L., Sharma, S., Yadav, C.S., Selvan, R.K., 2021. Understanding the relationship between the local crystal structure and the ferrimagnetic ordering of $Co_xMn_{3-x}O_4$ (x = 0–0.5) solid solutions. Journal of Alloys and Compounds, 853: 157256.
Ravel, B., Newville, M., 2006. ATHENA and ARTEMIS: Interactive graphical data analysis using IFEFFIT. Physica Scripta, 2005(T115): 1007.
Rehr, J.J., Albers, R.C., Zabinsky, S.I., 1992. High-order multiple-scattering calculations of x-ray-absorption fine structure. Physical Review Letters, 69(23): 3397-3400.
Şahin, B., Aydin, R., Cetin, H., 2020. Tuning the morphological, structural, optical and dielectric properties of hausmannite (Mn_3O_4) films by doping heavy metal lead. Superlattices and Microstructures, 143: 106546.
Shannon, R., 1976. Revised effective ionic radii and systematic studies of interatomic distances in halides and chalcogenides. Acta Crystallographica Section A, 32(5): 751-767.
Shaughnessy, D.A. et al., 2003. Molecular interfacial reactions between Pu(VI) and manganese oxide minerals manganite and hausmannite. Environmental Science & Technology, 37(15): 3367-3374.
Sherman, D.M., 1984. The electronic structures of manganese oxide minerals. American Mineralogist, 69(7-8): 788-799.
Song, B., Cerkez, E.B., Elzinga, E.J., Kim, B., 2020. Effects of Ni incorporation on the reactivity and stability of hausmannite (Mn_3O_4): Environmental implications for Mn, Ni, and As solubility and cycling. Chemical Geology, 558: 119862.
Spencer, C.D., Schroeer, D., 1974. Mössbauer study of several cobalt spinels using Co^{57} and Fe^{57}. Physical Review B, 9(9): 3658-3665.
Sukhdev, A. et al., 2020. Synthesis, phase transformation, and morphology of hausmannite Mn_3O_4 nanoparticles: photocatalytic and antibacterial investigations. Heliyon, 6(1): e03245.
Valldor, M., Andersson, M., 2002. The structure of the new compound $YBaCo_4O_7$ with a magnetic feature. Solid State Sciences, 4(7): 923-931.
Wilk, P.A., Shaughnessy, D.A., Wilson, R.E., Nitsche, H., 2005. Interfacial interactions between Np(V) and manganese oxide minerals manganite and hausmannite. Environmental Science &

624 Technology, 39(8): 2608-2615.
625 Xu, H., Xu, S., Wang, H., Yan, H., 2005. Characterization of hausmannite Mn_3O_4 thin films by chemical
626 bath deposition. Journal of The Electrochemical Society, 152(12): C803.
627 Yin, H. et al., 2014. Effects of Co and Ni co-doping on the structure and reactivity of hexagonal birnessite.
628 Chemical Geology, 381: 10-20.
629 Yin, H. et al., 2013. Effects of Fe doping on the structures and properties of hexagonal birnessites -
630 Comparison with Co and Ni doping. Geochimica Et Cosmochimica Acta, 117: 1-15.
631 Yin, H. et al., 2011. Co^{2+}-exchange mechanism of birnessite and its application for the removal of Pb^{2+}
632 and As(III). Journal of Hazardous Materials, 196: 318-326.
633 Yin, H. et al., 2015. High Co-doping promotes the transition of birnessite layer symmetry from
634 orthogonal to hexagonal. Chemical Geology, 410: 12-20.
635 Yin, H. et al., 2020a. Effects of Co(II) ion exchange, Ni(II)- and V(V)-doping on the transformation
636 behaviors of Cr(III) on hexagonal turbostratic birnessite-water interfaces. Environmental
637 Pollution, 256: 113462.
638 Yin, H. et al., 2012. Characterization of Ni-rich hexagonal birnessite and its geochemical effects on
639 aqueous Pb^{2+}/Zn^{2+} and As(III). Geochimica Et Cosmochimica Acta, 93: 47-62.
640 Yin, H. et al., 2020b. Preference of Co over Al for substitution of Fe in goethite (α-FeOOH) structure:
641 Mechanism revealed from EXAFS, XPS, DFT and linear free energy correlation model.
642 Chemical Geology, 532: 119378.
643 Zhang, F., Zhang, X.G., Hao, L., 2011. Solution synthesis and electrochemical capacitance performance
644 of Mn_3O_4 polyhedral nanocrystals via thermolysis of a hydrogen-bonded polymer. Materials
645 Chemistry & Phylogy, 126(3): 853-858.
646 Zhao, Q., Yan, Z., Chen, C., Chen, J.J.C.R., 2017. Spinels: Controlled preparation, oxygen
647 reduction/evolution reaction application, and beyond. Chemical Reviews, 117(15): 10121.
648 Zhao, Y., Li, C., Li, F., Shi, Z., Feng, S., 2011. One-step synthesis of highly water-dispersible Mn_3O_4
649 nanocrystals. Dalton Trans, 40(3): 583-8.
650

651 **Table 1.** Co K-edge EXAFS structural parameters obtained from the fit of Co-doped
652 hausmannites.

Octahedron	CoH5	CoH10
Co-O		
CN[a]	6	6
R (Å)[a]	1.968	1.970(12)
σ^2 (Å^2)[a]	0.0067(12)	0.0072
Co-Mn(Co)$_{OESx}$[b]		
CN	2	2
R (Å)	2.821(65)	2.798(43)
σ^2 (Å^2)	0.0110(63)	0.0113(35)
Co-Mn(Co)$_{OESz}$[b]		
CN	4	4
R (Å)	3.023(44)	3.005(29)
σ^2 (Å^2)	0.0110(63)	0.0113(35)
Co-Mn(Co)$_{OTCSx}$[b]		
CN	4	4
R (Å)	3.360	3.383(19)
σ^2 (Å^2)	0.0068(30)	0.0055(11)
Co-Mn(Co)$_{OTCSz/TT}$[b]		
CN	2	2
R (Å)	3.779(24)	3.771(19)
σ^2 (Å^2)	0.0011(17)	0.0032(17)
E_0 (eV)	-3.4(33)	-1.9(21)
Chi Sq.	126.39	91.27
R factor	0.0617	0.0233

653 Notes: [a]CN = coordination number; R = interatomic distance; σ^2 = Debye–Waller factor;
654 E0 = energy shift; Chi Sq. = chi-squared statistic.
655 [b]OES_x and OES_z refer to edge-sharing octahedra in the x- and z-axis; $OTCS_x$ and
656 $OTCS_z$ refer to octahedron-tetrahedron corner-sharing pairs in the x- and z-axis; TT
657 refers to the nearest tetrahedron-tetrahedron pairs.
658

Table 2. Electron structure, octahedral coordination radius (CR), electronegativity (χ), ionization potential (η), crystal field stabilization energy (CFSE), pairing energy (P) and bond dissociation energy (BDE) of Mn and Co.

Cation		Electronic structure		Configuration	CR (Å)[a]	χ[b]	η[c] (eV)	Δ[d] (kJ/mol)	CFSE[d] (kJ/mol)	P[e] (kJ/mol)	BDE[c] (kJ/mol)
Mn	II	$3d^5$	4(LS)	$(e)^4(t_2)^1$	—	—	33.7	39.8	79.6	285.0	362 ± 25
			4(HS)	$(e)^2(t_2)^3$	0.80	1.4934			0		
			6(LS)	$(t_{2g})^5$	0.81	1.4903		89.8	179.6		
			6(HS)	$(t_{2g})^3(e_g)^2$	0.97	1.4407			0		
	III	$3d^4$	4(LS)	$(e)^4$	—	—	51.2	111.6	290.2	301.6	
			4(HS)	$(e)^2(t_2)^2$	—	—			67.0		
			6(LS)	$(t_{2g})^4$	0.72	1.7052		251.3	402.1		
			6(HS)	$(t_{2g})^3(e_g)^1$	0.785	1.6753			150.8		
Co	II	$3d^7$	4(LS)	$(e)^4(t_2)^3$	—	—	33.5	48.9	58.7	250	397 ± 9
			4(HS)	$(e)^4(t_2)^3$	0.72	1.5882			58.7		
			6(LS)	$(t_{2g})^6(e_g)^1$	0.79	1.5665		110.1	198.2		
			6(HS)	$(t_{2g})^5(e_g)^2$	0.885	1.5371			88.1		
	III	$3d^6$	6(LS)	$(t_{2g})^6$	0.685	1.7913		248.4	534.2	282.6	
			6(HS)	$(t_{2g})^4(e_g)^2$	0.75	1.7614			89.0		

[a] Data adopted from Shannon (1976). [b] Data calculated according to Portier et al. (1994).

[c] Data from Lide and"Mickey" Haynes. (2010).

[d] Data from Burns (1993) and Huheey et al. (1993). These data were calculated by neglecting the electron pairing energies and electron-electron effects for simplification.

[e] Data from Huheey et al. (1993). These values are for the free ions and may be 15-30% smaller when cations are chemically coordinated because of the nephelauxetic effects.

669 **Figure Captions**

670 **Fig. 1** (a) Powder XRD patterns of HM and Co-doped hausmannite samples, overlaid
671 with the best Rietveld structure refinement results based on a hausmannite model (ICSD
672 76088). (b) Powder XRD patterns of three years aged Co-doped samples, agedHM and
673 agedCoH10, overlaid with the best calculated patterns by quantitative phase analysis
674 using a hausmannite model (ICDD 76088) and manganite model (ICSD 84949). Blue
675 lines are experimental data (Y_{obs}), red lines are calculated patterns (Y_{calc}), and the light
676 gray lines are the difference patterns (Diff)). The reflections of hausmannite are not
677 labeled while the main peak for manganite (γ-MnOOH) is indicated by dash line. (c)
678 Crystal diagram of hausmannite (ICSD 76088).

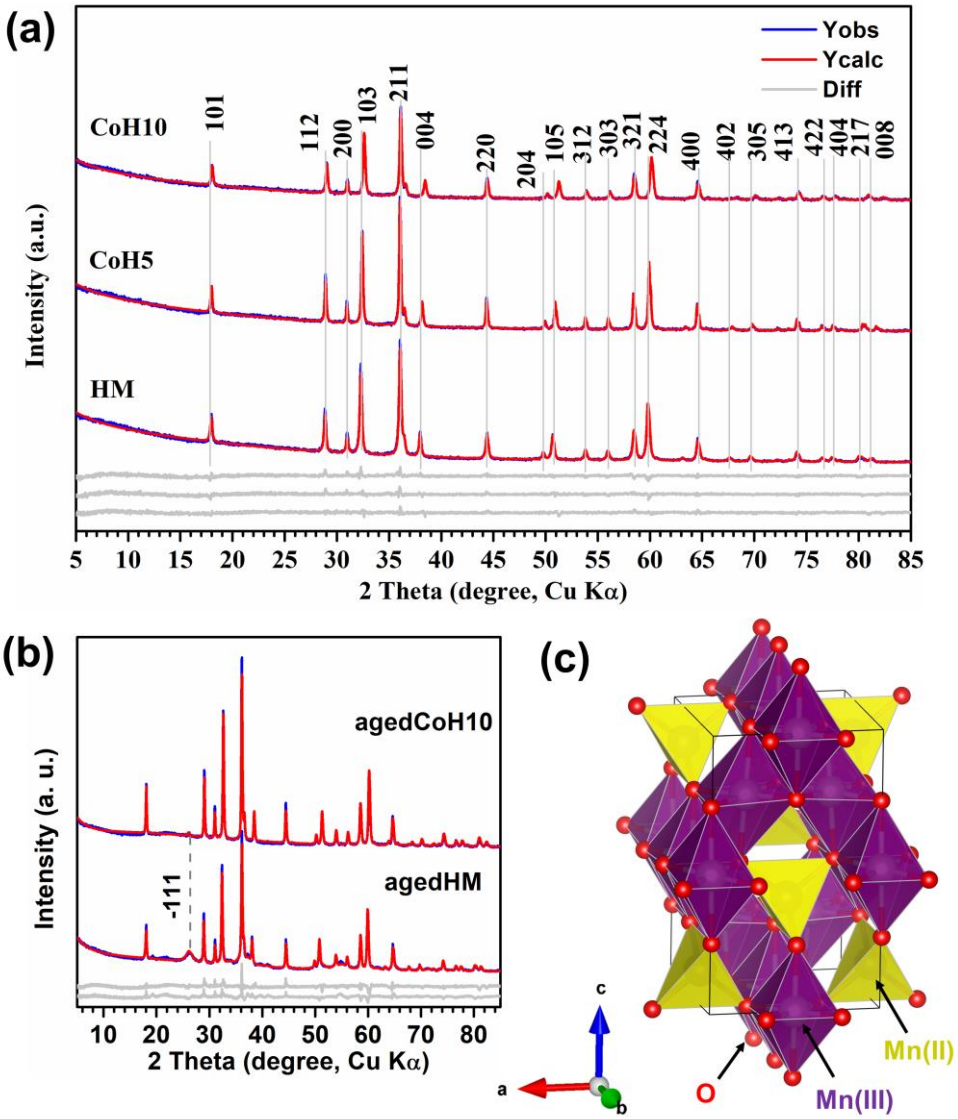
679 **Fig. 2** Typical TEM images of freshly prepared Co-doped hausmannite samples (a, HM;
680 b, CoH5; c, CoH10), and 3 years aged samples of (d) agedHM and (g) agedCoH10. (e)
681 and (i) show the SAED patterns of the areas in the blue rectangles in (d) and (g),
682 respectively, while (f) and (h) are typical HRTEM images for the area in the blue circle
683 in the inset at right down of panel (f) and the blue rectangle in panel (g) correspondingly.

684 **Fig. 3** FTIR spectra of freshly prepared and 3 years aged Co-doped hausmannite
685 samples and a synthesized manganite standard.

686 **Fig. 4** Mn 2p spectra of HM and CoH10 (a), and the corresponding Mn $2p_{3/2}$ spectra (b,
687 c) with the best fit overlaid (The black open circles represent experimental data, red
688 lines are the best fit to the data, peaks corresponding to Mn^{2+}, Mn^{3+} and Mn^{4+} are shown
689 as green dot, dash and solid lines respectively, and the gray solid lines at the bottom are
690 the difference patterns). (d) Linear combination fitting (red dashed lines) of Co K-edge
691 XANES spectra of CoH5 and CoH10, using $CoSO_4$ and CoOOH (Yin, 2015 #50) as
692 references.

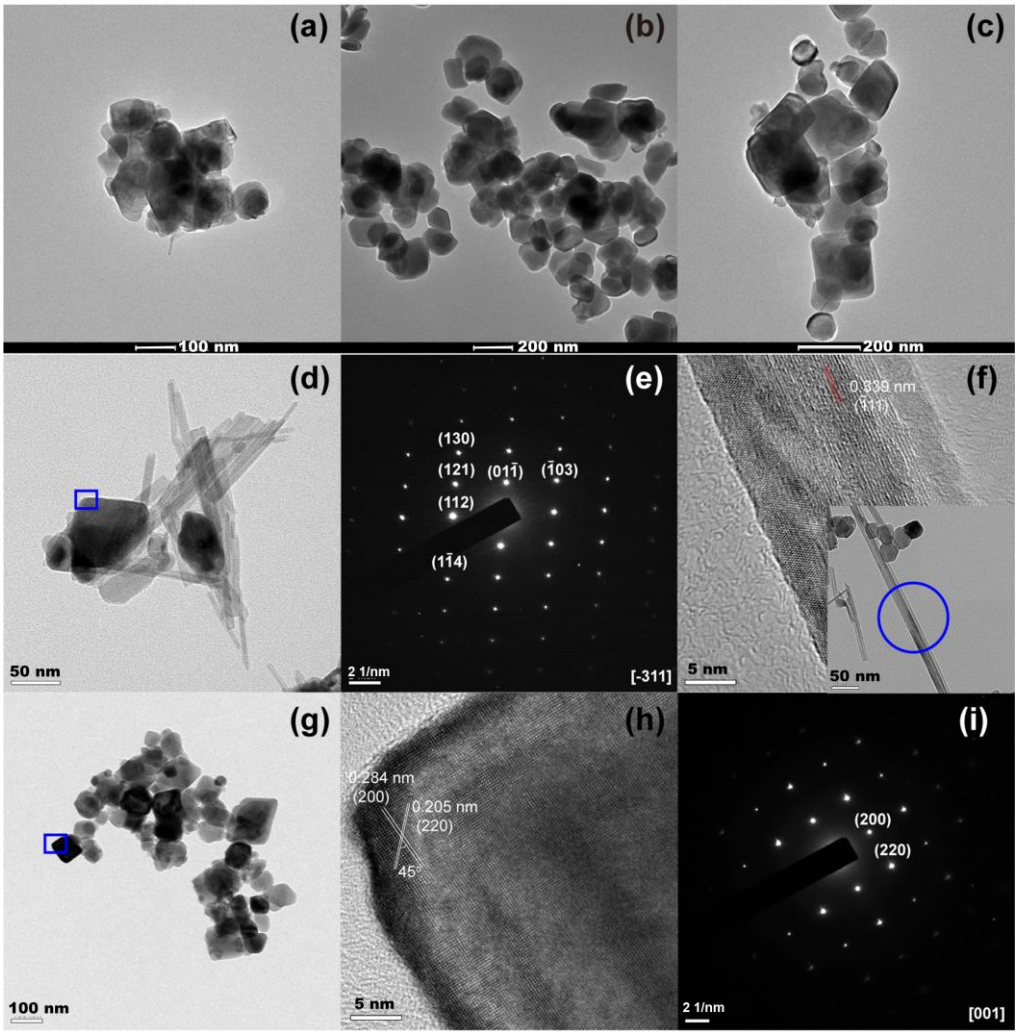
693 **Fig. 5** (a) Mineral dissolution kinetic curves expressed as %Co dissolved (χ_{Co}) or %Mn
694 dissolved (χ_{Mn}) in 2 M HCl solution at 25 ^{o}C and (b) the corresponding χ_{Co} versus χ_{Mn}
695 curves of these Co-doped hausmannite samples. In panel a, the inset is the detailed
696 figure in the first 12 h of the dissolution reactions, the solid lines are the best fit of the
697 whole dissolution curve with Kabai equation, $\chi_{Co(Mn)} = 1 - \exp(-(kt)^{\alpha})$, in which k and
698 α are constants representing the dissolution rate constant and the characteristics of the

699 mineral structure, and the corresponding fitting parameters are listed in the table
700 inserted in the panel. In panel b, the red solid line is the 1:1 line.
701 **Fig. 6** Comparison of k^3-weighted Co K-edge EXAFS (a) and the corresponding
702 Fourier transformed (FTs) spectra (b) of CoH10 and that of synthesized $CoSO_4$ and
703 CoOOH from our previous study (Yin et al., 2015). In panel b, the magnitudes of first
704 Co-O peaks were normalized. The Co K-edge EXAFS (c) and the corresponding
705 Fourier transformed (FTs) spectra (d) of CoH5 and CoH10, overlaid with the best fitting
706 by assuming that all the Co cations occupy the octahedral sites. Blue lines are
707 experimental data and dashed red lines are the best fits.
708 **Fig. 7** Comparison of the $c/\sqrt{2}a$ of the Co-doped hausmannite samples in the present
709 study with those of the $Mn_{3-x}Co_xO_4$ nanoparticles from previous studies (Bordeneuve
710 et al., 2010; Hirai et al., 2016; Rajeesh Kumar et al., 2021). The solid lines represent
711 the linear fitting of these data with $x < 1$.
712


(a)
Yobs
Ycalc
Diff
CoH10
CoH5
HM
101
112
200
103
211
004
220
204
105
312
303
321
224
400
402
305
413
422
404
217
008
Intensity (a.u.)
5 10 15 20 25 30 35 40 45 50 55 60 65 70 75 80 85
2 Theta (degree, Cu Kα)
(b)
agedCoH10
agedHM
-111
Intensity (a. u.)
10 20 30 40 50 60 70 80
2 Theta (degree, Cu Kα)
(c)
c
a
b
Mn(II)
O
Mn(III)

713

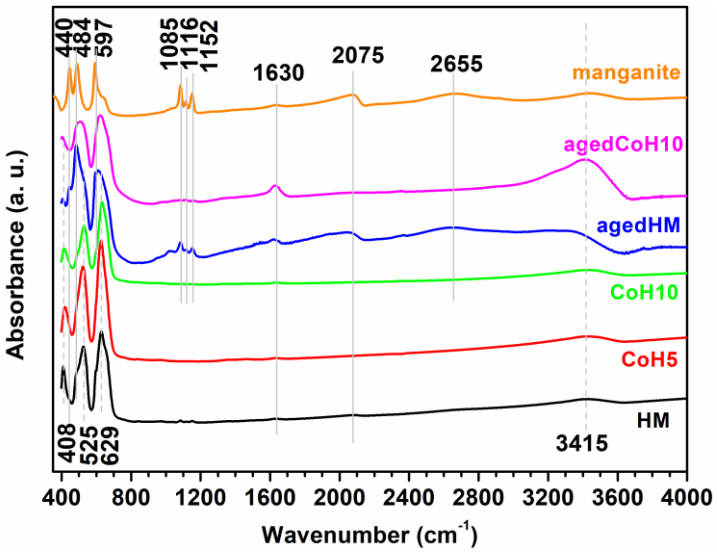
714 **Fig. 1**



715

716 **Fig. 2**

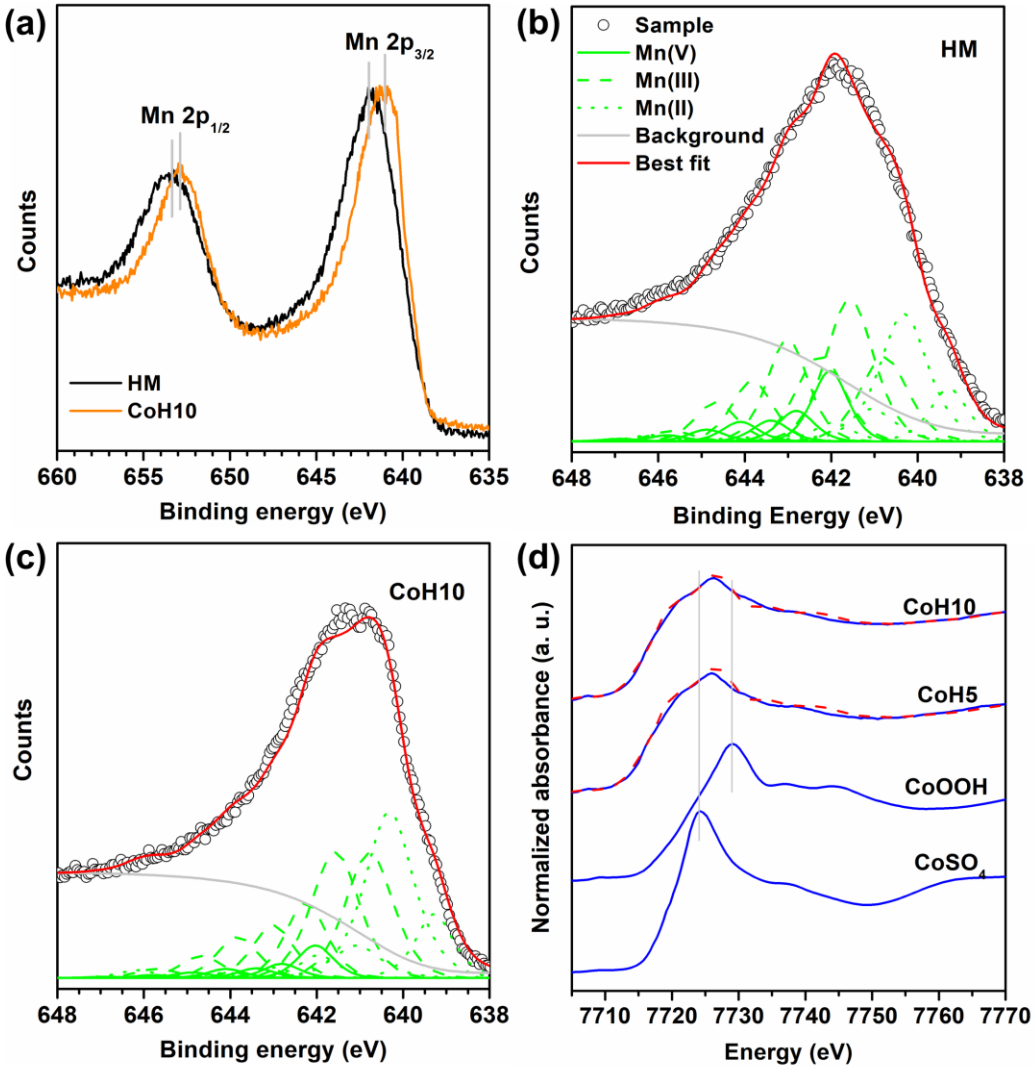
717



718

719 **Fig. 3**

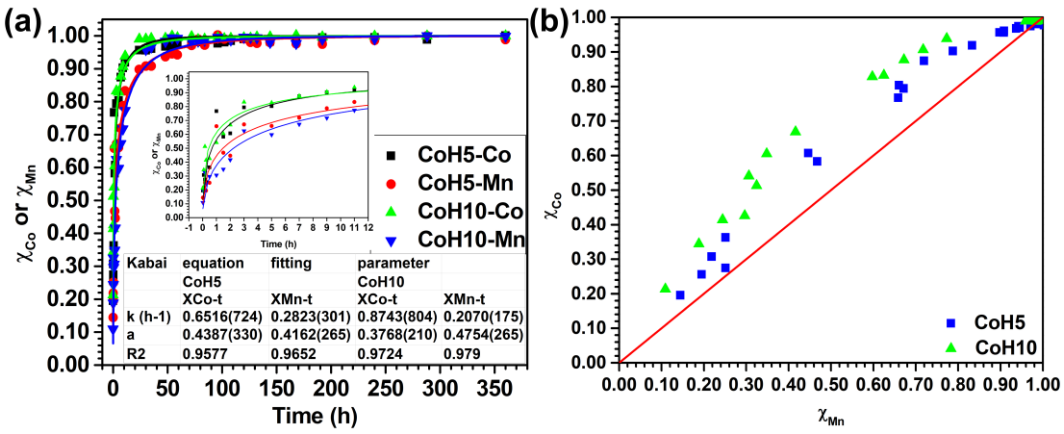
720



721

722 **Fig. 4**

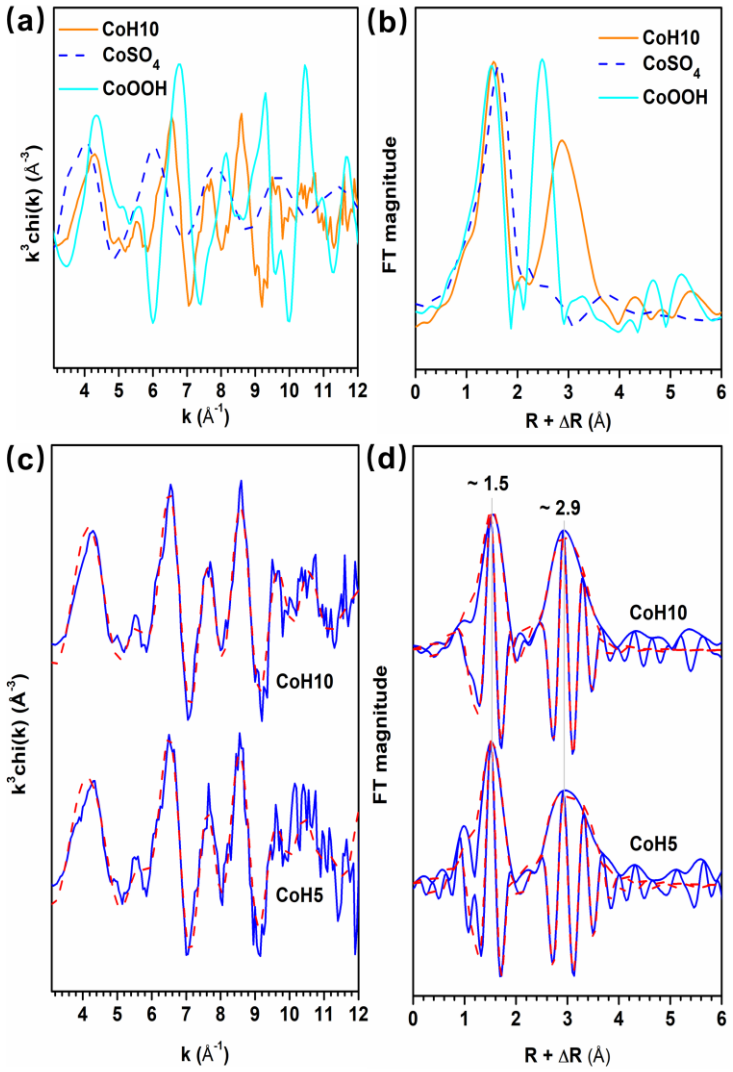
723



724

725 **Fig. 5**

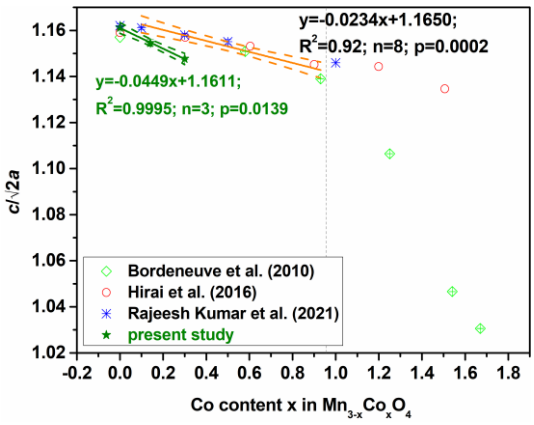
726



727

728 **Fig. 6**

729


y=-0.0234x+1.1650;
R2=0.92; n=8; p=0.0002
y=-0.0449x+1.1611;
R2=0.9995; n=3; p=0.0139
Bordeneuve et al. (2010)
Hirai et al. (2016)
Rajeesh Kumar et al. (2021)
present study
c/√2a
Co content x in Mn3-xCoxO4
1.16
1.14
1.12
1.10
1.08
1.06
1.04
1.02
-0.2
0.0
0.2
0.4
0.6
0.8
1.0
1.2
1.4
1.6
1.8

730

731 **Fig. 7**